Point detection in textured ultrasound images

Stine Hverven Thon [a,*], Andreas Austeng [a], Roy Edgar Hansen [a,b]

[a] *Department of Informatics, University of Oslo, P.O. Box 1080, Blindern, Oslo, NO-0316, Norway*
[b] *Norwegian Defence Research Establishment (FFI), P.O. Box 25, Kjeller, NO-2027, Norway*

ARTICLE INFO

ABSTRACT

Detection of point scatterers in textured ultrasound images can be challenging. This paper investigates how four multilook methods can improve the detection. We analyze many images with known point scatterer locations and randomly textured backgrounds. The *normalized matched filter* (NMF) and *multilook coherence factor* (MLCF) methods are normalized methods that do not require any texture correction prior to detection analysis. They are especially propitious when optimal texture correction of the ultrasound images is difficult to obtain. The results show *significant* improvement in detection performance when the MLCF method is weighted with the prewhitened and texture corrected image. The method can be applied even when we do not have prior knowledge about the optimal prewhitening limits. The multilook methods NMF and *NMF weighted* (NMFW) are very favorable methods to apply on images where acoustic noise dominates the speckle background.

1. Introduction

Detection of point scatterers in medical ultrasound is essential in several applications. Some example applications are detection of breast microcalcifications [1–6], kidney stones [7,8], microbubbles [9,10], and point tracking [11–13]. Peaks in the textured speckle background can make it very challenging to detect point targets. This paper investigates if four multilook methods have the potential to improve the point detection of a textured, standard Delay-and-Sum (DAS) image. The four multilook methods are introduced in [14], which studied uniform speckle backgrounds. We now assess the point detection performance of these methods on textured ultrasound images.

We can adjust the aperture weightings of the ultrasound array to optimize the signal to noise ratio (SNR) versus the peak sidelobe levels [15]. The results in [14] show how we can significantly improve the detection probability and increase the effective spatial resolution of the image if we apply an optimized *whitening* transform. Whitening has previously been used in ultrasound to improve detection of edges [16,17] or point scatterers in uniform speckle backgrounds [14]. This work studies the point detection performance of prewhitening combined with texture correction. To get measurable and statistically significant results, we simulate several images of a point scatterer in inhomogeneous speckle backgrounds using the Field II software [18–20]. An inhomogeneous texture predominantly has the same tissue type with some fluctuations about a mean value [21, ch. 9.2].

The methods in this paper are inspired by multilook techniques from the radar field [22–25]. In a similar fashion, Masoom et al. detect simulated spherical targets in textured ultrasound images by combining an algorithm from radio astronomy with constant false alarm rate (CFAR) processing from the radar field in [26]. The multilook technique is used on synthetic aperture radar (SAR) images and has the potential to reduce speckle [27, ch. 3.3] [28, p.29]. The method splits the entire frequency bandwidth of the original image into subsets. The subsets do not have the same central frequencies. We can in this way get many images or *sublooks* from one original image. The contribution from some of the sublooks are more important in terms of point detection. The *normalized matched filter* (NMF) multilook method maximizes point detection by imposing higher weighting on these sublooks [22–25]. We presented three new multilook methods to improve point detection in [14]. The *multilook coherence factor* (MLCF) [14] calculates the ratio between the coherent and incoherent sum of the sublooks with equal sublook weighting. It is a simpler method than the NMF method. The NMF and MLCF are normalized methods and do not require texture correction prior to detection analysis. The *normalized matched filter weighted* (NMFW) and the *multilook coherence factor weighted* (MLCFW) methods weight the NMF and MLCF methods with the prewhitened *and* texture corrected DAS image.

The performance of the multilook methods is benchmarked against texture corrected versions of the original and prewhitened DAS image. The MLCF and MLCFW methods do not need prior knowledge of the theoretical point signal response. By using suboptimal or wide prewhitening limits, we test the methods when the optimal whitening limits are unknown. We also evaluate the methods when a successful

---

* Corresponding author.

E-mail address: stinemhv@ifi.uio.no (S.H. Thon).

texture correction is difficult to obtain. Finally, we evaluate the multilook methods on images where acoustic noise dominates the speckle background.

Section 2 briefly describes how to measure point detection performance, and how to apply prewhitening and the multilook methods. We discuss how to estimate and correct for texture in Section 3. Section 4 presents the setup for the simulation and detection study. Section 5 presents the detection results for the methods and Section 6 discusses the observed performances on textured backgrounds.

2. Background

2.1. Point detection

We measure detection performance using the probability of false alarm P_{FA} and the probability of detection P_D. We estimate P_{FA} using images containing only speckle, and we estimate P_D using images with a point scatterer present [29, ch. 3.3]. We have a simulated environment with known location for the point scatterer and adopt the detection strategy from [30]. We evaluate a search window around the known point location, and pick the maximum value within it. The point's SNR metric [14,30] is the point's relative intensity compared to the background and it greatly affects P_D. We calculate the average intensity of the background around the point location using the speckle images without the point scatterer present.

A Receiver Operating Characteristics (ROC) curve displays detection performance by comparing P_D to P_{FA} for a given threshold γ [31, ch. 2.4.2] [29, p. 74]. As in [14,30], this paper presents ROC curves for P_{FA} values up to 0.1. ROC results can also be presented by tabulating P_D for a chosen P_{FA} value or the Area Under the Curve (AUC) [32, p. 315]. The accuracy of the ROC and AUC depend on the number of realizations [29, p. 37][30,33].

2.2. The whitening transform and spatial frequency limits

Whitening or prewhitening is an operation performed on a signal to make it more similar to white noise, and thus more suitable to be analyzed by statistics-based methods [34, p. 399]. A whitening transform can be estimated using a secondary data set or by applying an adaptive method. In this study we have simulated many realizations of speckle background images. We estimate the smoothed average of the spatial frequency spectrum used in the whitening transform from the simulated realizations. For most of the scenarios in this study, we estimated the average spectrum using the image speckle scenes without texture or after texture correction. A texture corrected image is an image where the amplitude variation of the speckle is estimated and corrected for, i.e., an image with almost uniform speckle background. We then apply the inverse of the smoothed average to the Fourier transform of the image in question. We refer to the resulting image as a whitened or prewhitened image in this study. The results in [14] illustrate the *significant* improvement in point detection obtained with an optimized whitening transformed image.

A system's imaging capability is governed by the point spread function (PSF) and many parameters affect it [35,36]. The spatial frequency spectrum is centered on $2k_0 = 4\pi f_0/c$ [37, ch. 3], where f_0 is the center frequency and c is the speed of sound. The aperture size limits the lateral spatial frequency k_x and the critical angle α [14,36,38,39]. The images in this study are bandpass filtered using lower and upper frequency limits f_L and f_H, i.e., $f_L \leq f \leq f_H$, and demodulated using the estimated center spatial frequency k_D ($k_D \approx 2k_0$). As in [14], we ensure uniform image resolution by applying an adaptive aperture setting with a range-independent beamwidth. The $f_\#$ is the ratio between imaging depth and active aperture size [21, p. 381]. We used an $f_\#$ of 1.75, and the reconstructed images are 20 mm wide with imaging depth of 20 mm to 60 mm. We use the notation κ_x and κ_z for the normalized spatial frequencies in the lateral and depth direction.

2.3. The multilook methods

The multilook technique is widely used on synthetic aperture radar (SAR) images [27, ch. 3.3] [28, p. 29]. It splits the frequency bandwidth of the original image into many subsets. The subsets have different central frequencies and they can either be independent or partially overlapping [25]. We create a sublook by computing the inverse Fourier transform of a subset. As in [14], we choose to apply L independent, non-overlapping, and uniformly spaced subsets to create sublooks with equal image resolution. The multilook methods evaluate the L-dimensional sublook vector y that corresponds to each image pixel. The *normalized matched filter* (NMF) [22,23,40] and the *multilook coherence factor* (MLCF) [14] are calculated on prewhitened images and do *not* require any texture correction prior to detection analysis. For the case of independent sublooks, NMF is [14]

$$\text{NMF}(y) = \frac{|a^H y|^2}{(y^H y)(a^H a)}. \tag{1}$$

NMF weights the sublooks according to the theoretical point signal response a for each pixel in each sublook. If we weight all sublooks equally, the test in (1) changes to the ratio of the coherent and incoherent sum of all sublooks, i.e., MLCF [14]:

$$\text{MLCF}(y) = \frac{|1^H y|^2}{(y^H y)L} = \frac{|\sum_{n=1}^{L} y(n)|^2}{L \sum_{n=1}^{L} |y(n)|^2}. \tag{2}$$

We also apply NMF and MLCF as a weighting schemes to the prewhitened *and* texture corrected image, $\text{DAS}_{\text{whitened+TC}}$. We refer to these two methods as *NMF weighted* (NMFW) and *MLCF weighted* (MLCFW) images.

$$\text{NMFW}(y) = \text{NMF}(y) \cdot \text{DAS}_{\text{whitened+TC}}. \tag{3}$$

$$\text{MLCFW}(y) = \text{MLCF}(y) \cdot \text{DAS}_{\text{whitened+TC}}. \tag{4}$$

3. Textured scenes

3.1. Creating textured backgrounds

Ultrasound images typically include varying echo intensities in the tissue speckle. Living tissue is full of structure, movement, and organization on several length scales [21, ch. 9.1]. An *inhomogeneous* texture has the same type of tissue with small fluctuations about a mean value, while a region enclosing a group of regions with different characteristics is called *heterogeneous* [21, ch. 9.2]. An ultrasound image can have edges caused by transitions between interfaces or lines caused by anisotropic muscle fibers, making it more difficult to discern small point scatterers. An optimal point scatterer detector needs to handle nonuniform backgrounds.

As in [14], we simulate a huge number of images containing a single point scatterer at different positions and images containing uniform speckle. By combining all the different point only images with every speckle only image we produce a set of images of a point at different locations in speckle. By scaling the point only images we control the point SNR value in the final images. Combining the images is mathematically equivalent to combining the raw channel data since DAS is a linear process. We can also combine the DAS images with random texture maps to simulate textured backgrounds. The point scatterer will retain its point SNR compared to the immediate surrounding background. Point detection is particularly of interest within a tissue area, such as a liver or a cyst. We choose to model the tissue backgrounds with random texture fluctuations of a specific scale such that the size of the texture is larger than that of a point scatterer but substantially smaller than the image scene.

We create a frequency spectrum with a steep Gaussian profile with maximum value in the center. With a Gaussian texture profile, it is easy to set a specific scale for the texture blobs as the shape is of the form
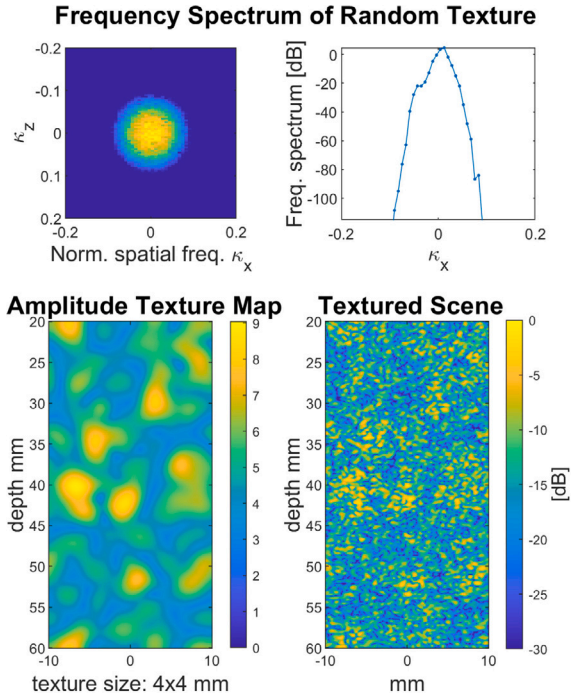
Fig. 1. Example of a random texture map. We first create a frequency spectrum with a Gaussian distribution and multiply this with a complex random frequency spectrum. An example is shown to the upper left, and a cut through the spectrum at κ_z is shown to the upper right. We form the amplitude texture map shown to the lower left by inverting the created spectrum. To get the textured scene to the lower right, we multiply the amplitude texture map with the original image. The final DAS image is normalized by its maximum value and shown with a 30 dB dynamic range.

$e^{-(k_z^2+k_x^2)/s_t}$, where s_t sets the scale of the texture fluctuations. We multiply this Gaussian profile with a complex random frequency spectrum and get the frequency spectrum shown in the upper subimages in Fig. 1. Since we simulate the texture, we can measure the texture's size using the frequency spectrum. The −6 dB width Δk_x in spatial frequency is related to the −6 dB width in the image domain

$$\Delta x_{\text{texture}} = \frac{2\pi}{\Delta k_x}. \tag{5}$$

Inversion back to the image domain creates the amplitude texture map. Fig. 1, bottom left, shows an example texture map with texture size is 4 mm × 4 mm, which we refer to as small texture size. We then multiply the amplitude texture map with the original DAS image to get the final textured image shown to the bottom right in Fig. 1. The left subimage in Fig. 2 shows a scene with large texture size of 8 mm × 9 mm.

3.2. Texture estimation and correction

Texture correction finds slowly varying changes in the amplitude of the textured image and removes them. This is a necessary step for simple threshold detection to work. Another option is to have the detector locally estimate the speckle level [29, ch. 9]. We find a texture estimate by first applying background smoothing with a sufficiently large window. The size of the texture must typically be estimated, which is not always easy to do. Since this is not a study about texture correction, we choose the texture scale estimated from the texture map to get the best possible texture correction. We start with median filtering and continue with a Gaussian smoothing kernel with filter size set to the measured −6 dB texture size. We obtain a texture corrected image by dividing the original image with the texture estimate. Fig. 2 shows the texture estimate of an image and the resulting texture corrected image.
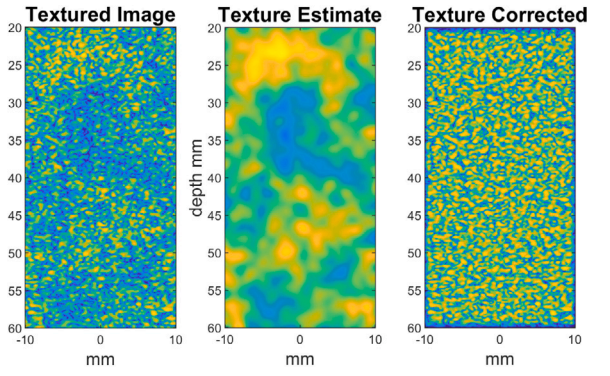

Fig. 2. Texture correction of the DAS image ("DAS TC") shown to the left. A texture estimate as shown in the middle is found by applying background smoothing with a large window. We obtain a texture corrected image as shown to the right by dividing the original image with the texture estimate. The texture estimate is shown with a 15 dB dynamic range, while the other images have a 30 dB dynamic range. The images are normalized by their maximum value to be comparable.
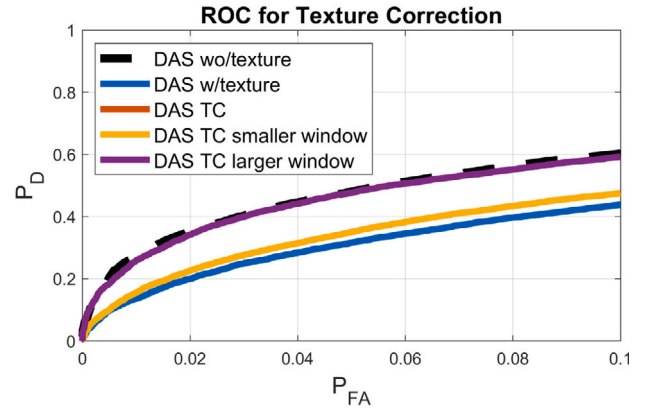

Fig. 3. ROC for texture corrected (TC) images using three window filter sizes compared to original DAS *with* and *without* texture. P_{FA} is shown up to 0.1. The red curve signifies TC using the measured −6 dB texture size. The red curve lies directly beneath the purple curve. The purple curve corresponds to 50% larger window size.

The optimal texture correction depends on the scale of the texture. The ultrasound image can have varying texture, and we must use adaptive filtering in such instances. This is not included in this study since we simplify the study to the same texture size in the whole image scene. The window size for texture estimation must be sufficiently large to avoid suppressing point scatterers but at the same time small enough to capture small scale texture variations. It can be challenging to estimate large texture variations of small scale. Fig. 3 compares the ROC results using varying window sizes to the original DAS images *without* texture and point SNR of 8.7 dB. Fig. 3 shows how texture degrades the ROC. Texture correction can improve the detection performance but will not entirely reach the same performance as non-textured backgrounds. Using a too small window size reduces P_{D} and creates a ROC curve only slightly better than applying no texture correction.

4. Methods

We created raw channel data using the Field II software, and performed the DAS beamforming using the Ultrasound Toolbox (USTB) [41] in MATLAB (Mathworks, Natick, MA). The simulation setup is a replica of the setup used in [14,30]. We used a linear array with 38.1 mm aperture size, consisting of 128 elements with λ pitch. The center frequency f_0 was 5.1 MHz, the speed of sound was 1540 m/s and the transmitted pulse had a frequency bandwidth of 65% of f_0. Hamming apodization was applied on transmit.
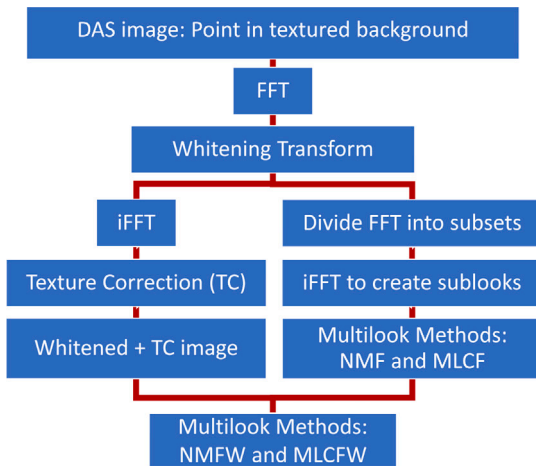
Fig. 4. Illustration of the detection analysis setup of this study on textured images. We first apply a whitening transform to the original, textured DAS image while in the spatial frequency (FFT) domain. We divide the frequency spectrum into subsets and create *sublooks*. We apply the multilook methods NMF and MLCF on these sublooks. To create the NMFW and MLCFW images, we multiply the multilook weights to the prewhitened *and* texture corrected image. We assess the point detection performance of the various methods.

As in [14,30], we simulated radio frequency channel data separately for the point scatterer and the speckle background. We simulated the speckle image using at least 20 scatterers per resolution cell, corresponding to 91 000 point scatterers in total per speckle realization. To obtain images with high, uniform spatial resolution, we used a synthetic transmit aperture setup with constant $f_\#$. Such a setup transmits from every consecutive element, receives on all elements, and synthesizes focus at every pixel. We do not include frequency dependent attenuation in the simulations. We coherently combine the resulting point and speckle images to obtain a final DAS image with a specific point SNR value. Using focused, uniform amplitude speckle scenes ensures the same point SNR value regardless of where in the scene the point target is located.

Fig. 4 shows the detection analysis setup. We simulated 243 focused, constant resolution, uniform amplitude speckle scenes and 117 single point images that were coherently combined to form 28 431 speckle scenes with a single point target. This defines our sample size for P_D and P_{FA} calculation in our detection performance study. Different from [14], this study uses textured backgrounds that more closely resembles a real-world situation. With uniform resolution, we can simplify the prewhitening process by assuming the same wavenumber coverage for all pixels. We calculated the point SNR value using the point scatterer in the center of the *untextured* DAS image. We chose a point SNR value signifying relatively weak point scatterers for the detection studies. The point SNR is 8.7 dB for the original untextured DAS image for all the scenarios under study except the dominant additive acoustic noise scenario. In the latter case, the original intensity of the point scatterer had to be increased to 9.5 dB for it not to be buried by the noise. Each ROC curve represents 28 431 realizations of one choice of point SNR value.

Before adding texture, we calculated correction maps from the average of all speckle backgrounds to ensure uniform average background intensity. The texture in this study is of two different sizes; 4 mm × 4 mm and 8 mm × 9 mm. We varied the texture amplitude to find an amplitude fluctuation that distinctly reduces the point detection performance. The distinct drop in ROC after multiplying the original image with the amplitude texture map is shown in Fig. 3 by the black and blue curves. The texture map in Fig. 1 shows the applied amplitude map that we multiplied to the original image. We also varied the window size for the texture estimation, as illustrated in Fig. 3.

The *optimal* whitening limits depend on the geometry, system setup, and the SNR [14]. We also tested the multilook methods combined with *suboptimal* or *wide* whitening limits. Prewhitening suppresses subsets outside the whitening limits. We applied the following three whitening limits:

- Optimized: angle α with frequency limits $\{f_L, f_H\}$
- Suboptimal: $\alpha + 10\%$ with $\{-5\% f_L, +5\% f_H\}$
- Wide: $\alpha + 30\%$ with $\{-10\% f_L, +10\% f_H\}$

Acoustic noise is a realistic scenario as the imaging depth increases. As mentioned, a ROC study was also performed for dominant acoustic noise. To simulate the noise, we created channel data consisting of white Gaussian noise and basebanded it before beamforming. We then coherently combined the resulting noise image with the speckle background image. We applied an adaptive prewhitening for the noisy background scenario, where we estimated a smoothed average version of each image's spatial frequency spectrum and applied the optimal whitening limits. We created the point scatterer look vectors for the NMF method by simulating the actual response of a point scatterer placed in each pixel and the pixel's corresponding look vector [14]. We studied the following cases corresponding to realistic scenarios:

- Prewhitening before or after texture correction.
- Optimal prewhitening and texture correction. The optimal prewhitening limits and the optimal window size for texture estimation are both known.
- Varying texture size. How do the methods perform on small versus large texture size? Using optimal prewhitening and texture correction.
- Varying number of sublooks for the multilook methods. Using optimal prewhitening and texture correction.
- Suboptimal/wide prewhitening. The whitening limits are approximately known or estimated from the frequency spectrum of the image. Using optimal texture correction.
- Suboptimal texture correction. The optimal window size for texture estimation is not known. Using optimal prewhitening.
- Dominant additive acoustic noise. Using optimal texture correction and adaptive prewhitening with optimal whitening limits.

MLCF and MLCFW are especially of interest in the case of suboptimal prewhitening since they do not require any prior knowledge about the optimal limits and the theoretical point signal response in each sublook.

In Section 5.2, we present an example image of the methods applied on an experimental image acquisition of a CIRS 054GS tissue-mimicking phantom. The phantom is imaged with a Verasonics linear probe (L7-4) with 5.2 MHz center frequency and $f_\# = 1.7$. We note that we only include this example for illustrative purposes. The optimal spatial frequency bandwidth limits are unknown in this example case. The frequency bandwidth is estimated from the image's frequency spectrum, and the angular whitening limit is based on the imaging setup's $f_\#$. The more straightforward methods MLCF and MLCFW are compelling to use in this scenario since they do not need prior knowledge about the theoretical point signal response. The multilook methods used 19 × 15 sublooks.

5. Results

5.1. Prewhitening before or after texture correction

Fig. 2 illustrates texture correction of the DAS image, termed "DAS TC". Fig. 5 shows the results when the textured image is whitened *prior* to texture correction. We refer to this as "Whitening + TC" in the result figures.

Fig. 6 shows the difference in detection performance when whitening is applied before or after texture correction, termed "Whitening + TC" and "TC + Whitening". The red curve shows the ROC results of only applying texture correction to the DAS images, termed "DAS TC".
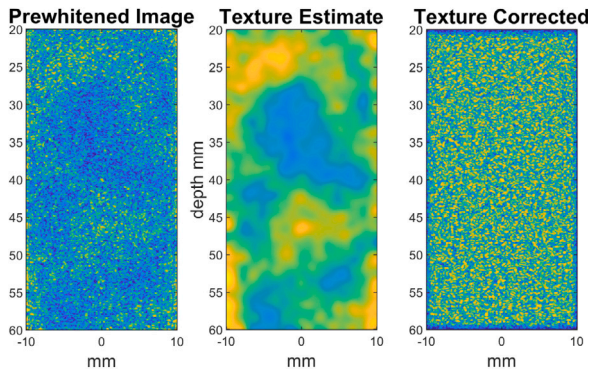
Fig. 5. Texture correction on a whitened image ("Whitening + TC"). We obtain the texture corrected image shown to the right by dividing the whitened image shown to the left with the texture estimate shown in the middle. The texture estimate is shown with a 15 dB dynamic range, while the other images have 30 dB dynamic range. The images are normalized by their maximum value to be comparable.
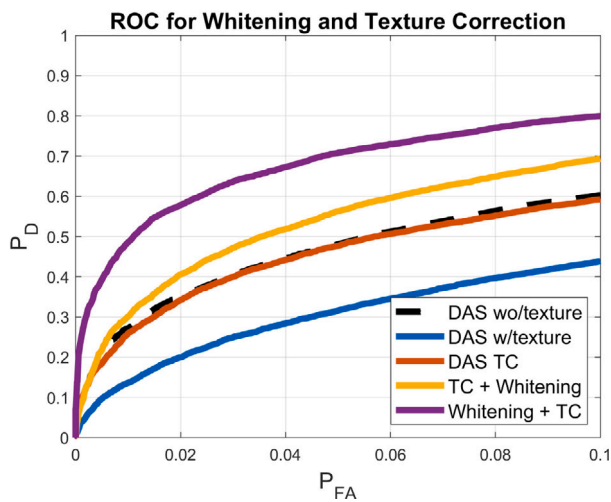

Fig. 6. ROC for texture corrected (TC) images compared to original DAS *with* and *without* texture. P_{FA} is shown up to 0.1. "DAS TC" signifies applying texture correction to the DAS image, whereas "Whitening + TC" signifies prewhitening and then texture correction.

5.2. Example images

We present two example images to illustrate the multilook methods on textured backgrounds. The first example is the textured ultrasound image in Fig. 7 with several point scatterers simulated using Field II software with the same setup as in the detection study. The optimal prewhitening limits and the optimal window size for texture estimation are both known in this example. Based on this image alone, it would seem the multilook methods are better suited for point detection. For example, at the −16.9 dB threshold, the MLCFW image has zero false alarms and retains all true positives. In comparison, the whitened image has zero false alarms at the −4.9 dB threshold. However, the methods could be stretching the dynamic range [42] and not actually improving the point detection. As discussed in [14], we must for this reason measure the detection performance using many independent images or realizations with known point scatterer locations.

The second example is an image of a tissue-mimicking phantom imaged and shown in Figs. 8 and 9. The original image is highly speckled and all four images are shown with a 21 dB dynamic range to be visually comparable. In the original DAS image, the amplitude difference between the two point targets is slight. However, the whitening process increases the intensity difference between the points to 5.6 dB.

We note that the optimal whitening filter was unknown and instead estimated from the frequency spectrum of the image. The multilook methods use the prewhitened image as input and the resulting figures further increase the difference between the points. As an example, the MLCF image has a 10 dB difference between the two point targets and thereby indicate that the bottom point scatterer is more likely to be a true point target. The MLCFW image has zero false alarms and retains both point scatterers at the shown −21 dB threshold. Again, we cannot ascertain which method is better suited for point detection from a few image examples. A detailed detection study requires many images with known point target locations and point SNR values.

5.3. Detection results on simulated images

The dashed black curve in Fig. 10 represents the texture corrected (TC) DAS images, as illustrated in Fig. 2. Point SNR is 8.7 dB for the original *untextured* DAS image for all the scenarios under study except the dominant additive acoustic noise scenario. The solid black curve shows the ROC curve for the prewhitened and textured corrected images ("Whitening + TC"), as illustrated in Fig. 5. The colored ROC curves represent the four multilook methods. Since low P_{FA} values are of interest, the ROC curves are shown for P_{FA} values up to 0.1. Fig. 10 presents the results for the multilook methods using 13×13 sublooks on images with large texture variations. This ROC study applied optimal α-prewhitening and optimal texture correction. Fig. 11 presents the corresponding AUC results.

Fig. 12 presents the detection performance of MLCFW using varying number of sublooks. Optimal prewhitening and optimal texture correction are applied in these cases. The optimal number of sublooks for the multilook methods on large texture is around 19×15, while the optimal on small texture is around 13×13 sublooks.

Fig. 13 presents the ROC results for the four multilook methods using suboptimal texture correction. The number of sublooks is 13×13, and the texture size is small. The window size used in texture correction is smaller than the actual texture size, and it therefore slightly degrades the overall detection performance of "Whitening+TC". All four multilook methods outperform prewhitening. Fig. 14 presents the corresponding AUC results. The multilook methods NMFW and MLCFW have the highest AUC values. Fig. 15 shows the P_D values given 3% P_{FA} for the multilook methods when a suboptimal, slightly wider whitening filter was used. Fig. 15 shows the P_D values when a filter with very wide whitening limits was used.

Fig. 17 presents the ROC results for the four multilook methods on images where additive acoustic noise dominates the speckle background. We applied adaptive prewhitening of the images. Optimal whitening limits and optimal window size for texture correction are both known. All four multilook methods perform better than prewhitening, especially the multilook methods NMFW and NMF. The number of sublooks is 19×15, and the texture size is large. The dotted, black ROC curve represents the original noisy DAS images without prewhitening and texture correction. The point SNR is 9.5 dB for the original *untextured* images. Fig. 18 presents the corresponding AUC results.

6. Discussion

Optimized prewhitening significantly improves the detection performance when combined with texture correction. Prewhitening prior to texture correction achieves a much higher detection performance than applying texture correction first, as shown in Fig. 6. This is because prewhitening improves spatial resolution, giving a larger scale difference between point scatterers and texture. This again allows for better texture correction without negatively affecting the point scatterer response. The AUC results for prewhitening are higher in the case of large texture. An optimal texture estimate is easier to achieve with slowly varying texture, such as in Fig. 5.
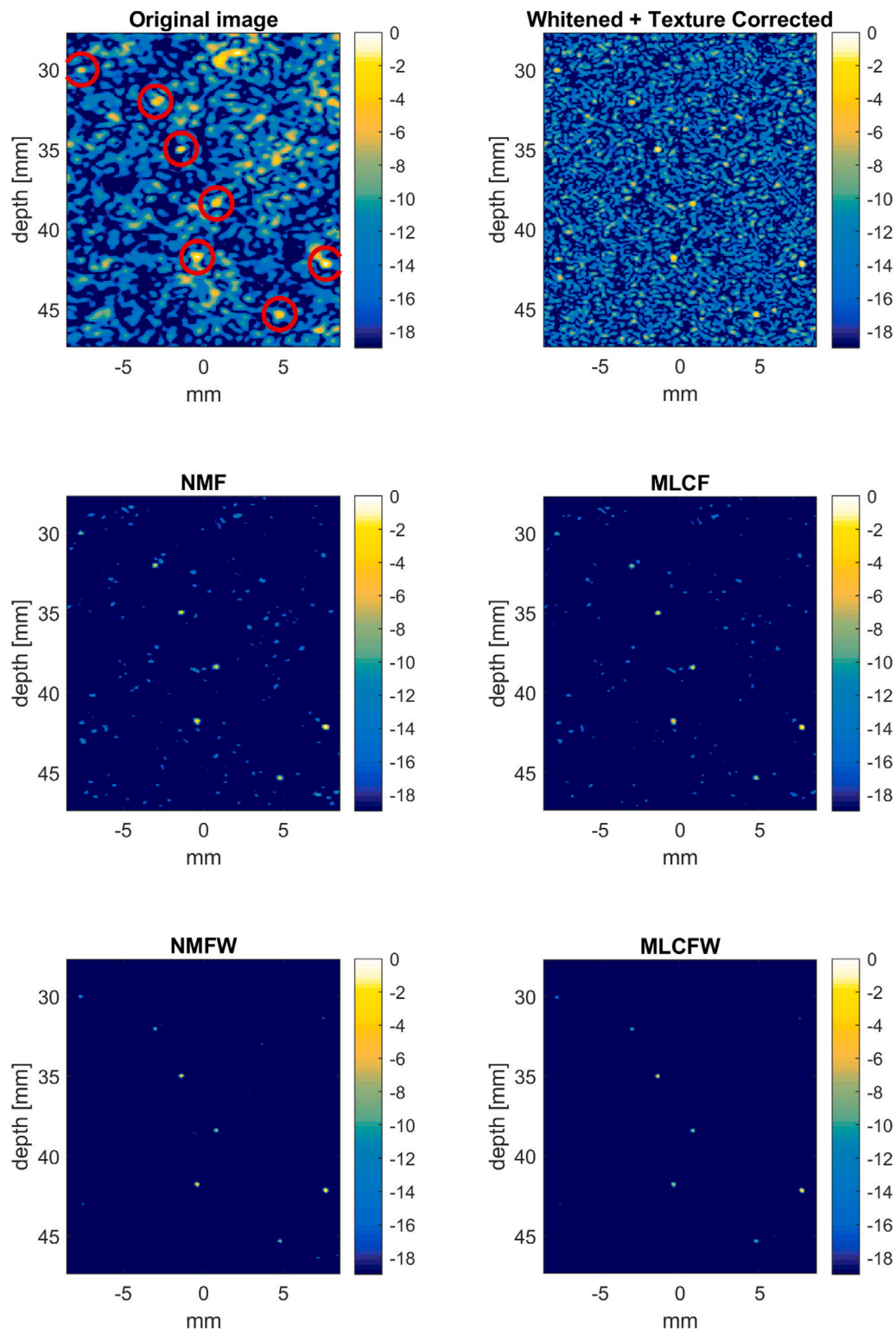
Fig. 7. Ultrasound image with seven point scatterers in a textured background. The red circles in the original DAS image indicate the locations of the true point scatterers. The multilook methods NMF, MLCF, NMFW, and MLCFW used 19 × 15 sublooks and α-prewhitening. To be visually comparable, the images are normalized by maximum and shown with a 19 dB dynamic range.

Prewhitening uses a classical spectral estimator, which requires that the input signal is stationary and ergodic [34, p. 399]. An amplitude trend in the data as a function of depth can be compensated by applying a time-varying gain or depth correction to remove the transmission loss effects before entering the spectral domain and applying prewhitening.

When the spectrum shape changes with depth, the signal is strictly non-stationary even after depth correction. A fixed prewhitening filter is then suboptimum, and a depth-dependent prewhitening filter can be applied. We expect the multilook methods to do better than prewhitening and texture correction in such cases. If the amplitude variations
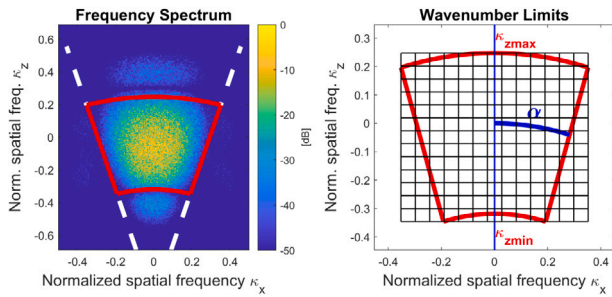
Fig. 8. Whitening filter limits for an ultrasound image of a tissue-mimicking phantom where the optimal frequency limits are unknown and must be estimated from the image's frequency spectrum. The angular limit is based on the $f_\#$. The chosen area is divided into subsets for the multilook methods.
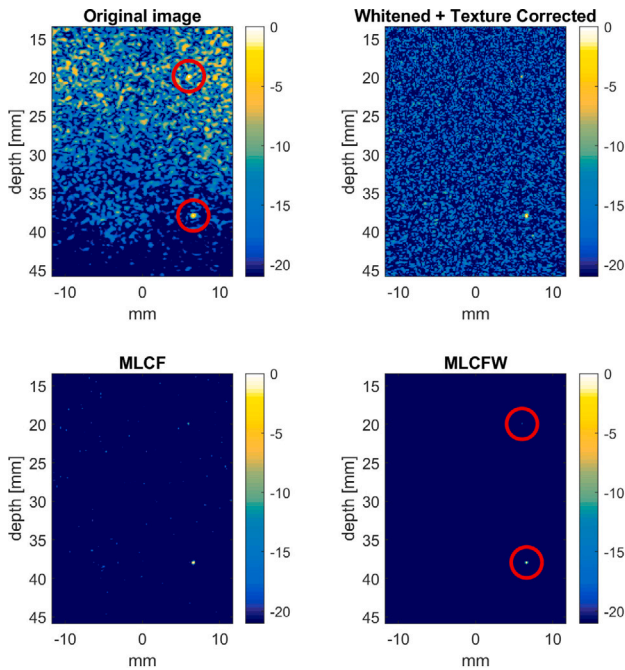

Fig. 9. An ultrasound image of a tissue-mimicking phantom with point scatterers in a highly speckled background. The original image is shown with the whitened and texture corrected image and the multilook methods MLCF and MLCFW. The whitening limits are estimated from the image's frequency spectrum. The red circles indicate the true point scatterers. To be visually comparable, the images are normalized by maximum and shown with a 21 dB dynamic range.

in the ultrasound image are considerable, it may be beneficial first to apply texture correction to achieve stationarity before applying prewhitening.

By comparing the AUC results in Fig. 12, it is evident that both prewhitening and the multilook methods perform better when the texture size is large. The results in Fig. 12 show how the multilook method improves its detection performance when the number of sublooks decreases. Table 1 summarizes the observed behavior of the multilook methods using a varying number of sublooks when applied to different image backgrounds. Fewer sublooks increases the calculation speed of the multilook method. Textured scenes require sublooks with higher image resolution than the uniform speckle backgrounds previously studied in [14]. The numerator in (1) retains full image resolution regardless of the number of sublooks. However, the denominator improves its background estimate when the sublooks are many but have high image resolution. Therefore, the optimal number of sublooks depends on the texture size. A small texture size requires subsets with larger bandwidth to be discernible in the resulting sublooks. The results
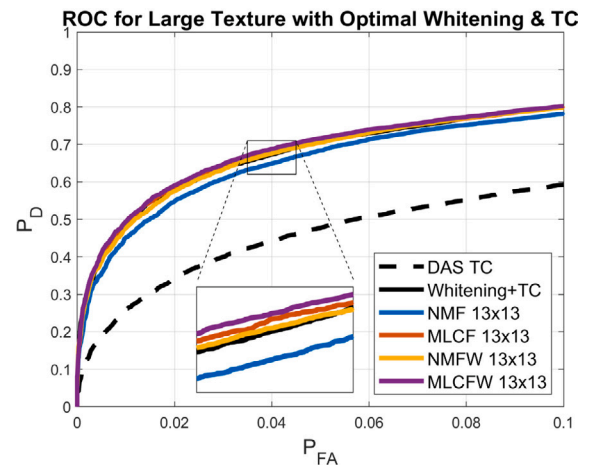

Fig. 10. ROC for the four multilook methods using 13×13 sublooks on images with large texture variations. Optimal α-prewhitening and optimal texture correction are applied.
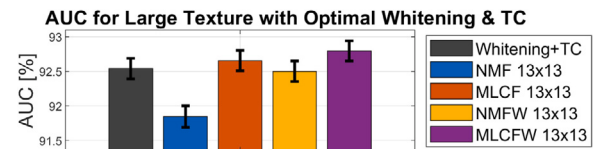

Fig. 11. AUC for the four multilook methods using 13×13 sublooks on images with large texture variations. Optimal α-prewhitening and optimal texture correction are applied.
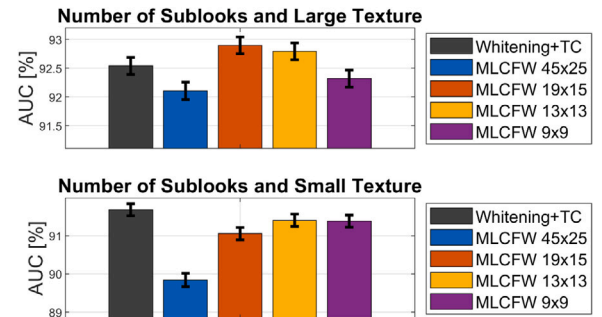

Fig. 12. AUC for the multilook method MLCFW using optimal "Whitening + TC" and a varying number of sublooks on images with small and large texture variations.
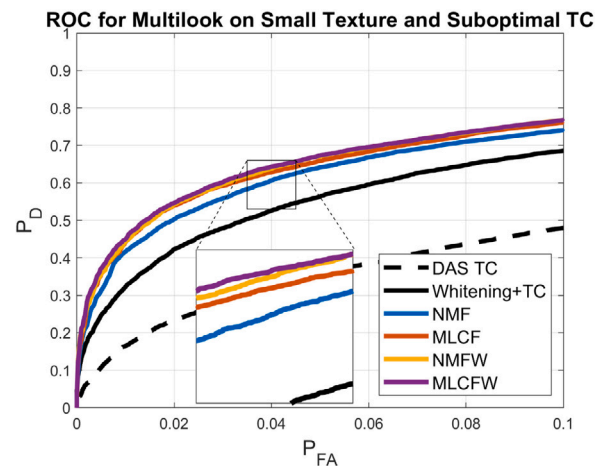

Fig. 13. ROC for the multilook methods on DAS images with suboptimal texture correction (TC). The texture size is small. The methods used 13×13 sublooks and optimal whitening.
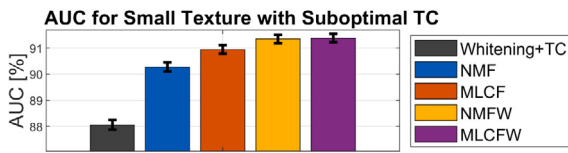
Fig. 14. AUC for the multilook methods when using suboptimal texture correction (TC). The texture size is small. The methods used 13×13 sublooks and optimal α-whitening.
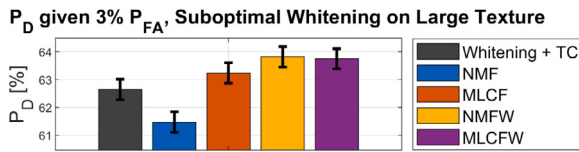

Fig. 15. P_D given 3% P_{FA} for the multilook methods using 19×15 sublooks combined with suboptimal prewhitening and optimal texture correction (TC).
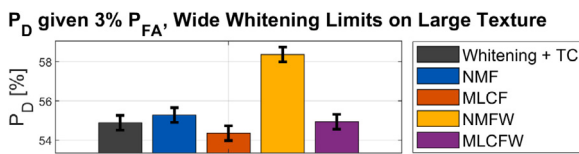

Fig. 16. P_D given 3% P_{FA} for the multilook methods using 25×21 sublooks combined with very wide whitening limits and optimal texture correction (TC).

Fig. 17. ROC for the multilook methods on DAS images with dominant acoustic noise and optimal texture correction. The texture size is large. The methods are calculated using 19×15 sublooks and adaptive prewhitening with optimal limits.
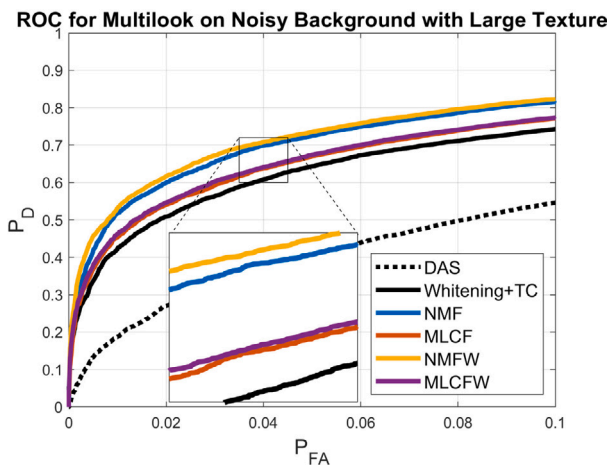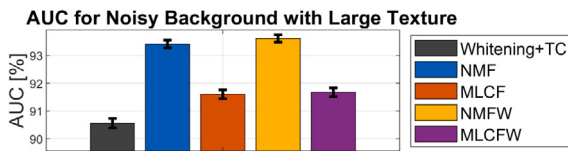

Fig. 18. AUC for the multilook methods on DAS images with dominant acoustic noise and optimal texture correction. The texture size is large. The methods are calculated using 19×15 sublooks and adaptive prewhitening with optimal limits.

for the multilook methods are better for slowly varying texture since we then can use a higher number of sublooks, which improves the denominator's estimate.

The results in Figs. 10, 14, and 18 show significant improvement in detection performance using the image weighted MCFW multilook

Table 1
Summary of number of sublooks.

Background	Number of sublooks			
	9×9	13×13	19×15	45×25
Homogenous	Poor	Poor	Moderate	Best
Large texture	Moderate	Good	Best	Poor
Small texture	Good	Best	Good	Poor

method. The benefit of MLCFW is that it can be applied even when prior knowledge about the theoretical point signal response and the optimal prewhitening limits is unavailable. Even for the scenario of optimal prewhitening and optimal texture correction in Fig. 10, the ROC curves for the MLCF and MLCFW methods slightly outperform prewhitening at low P_{FA} values.

The ROC study on suboptimal prewhitening in [14] found a significant improvement in detection performance for the multilook methods using 45×25 sublooks. The NMFW method performs better than MLCFW in the case of suboptimal whitening since it incorporates extra knowledge about the correct point signal response per sublook and can suppress more unwanted subsets at the edges of the spectrum. However, the inclusion of texture in this study causes the optimal number of sublooks to decrease. As a consequence, the multilook methods cannot suppress as many unwanted edge subsets, and therefore they cannot achieve the same amount of improvement as found in [14]. The results on suboptimal prewhitening on textured image scenes show that NMFW and MLCFW performs slightly better than prewhitening at low P_{FA} values, as illustrated by the P_D values in Fig. 15. The difference is however too small to give the multilook methods higher overall AUC values. Prewhitening is a robust method even when applied suboptimal limits. Fig. 16 illustrates a scenario when the whitening limits are poorly estimated and chosen too wide. The NMFW method performs much better than the other methods in this case. The number of sublooks is 25×21 to give subsets of similar size as when using the optimal prewhitening limits.

The image example in Fig. 7 makes it evident that the multilook methods can increase the threshold difference between false alarms and true positives. It is more challenging to visually extract the point scatterers in the whitened image than the multilook weighted images. Therefore, it can be preferable for an ultrasound operator to see the multilook images when searching for point scatterers.

The improvements in detection performance for the multilook methods compared to prewhitening are especially large for image backgrounds where optimal texture correction is difficult to obtain. This is shown in Figs. 13 and 14. An ultrasound image can have a varying texture scale, making it more challenging to obtain an optimal texture estimate. The image weighting methods NMFW and MLCFW perform best in Fig. 13 since the applied texture correction still provides some improvement to the detection performance. However, the NMF and MLCF methods show great potential when an optimal texture correction is difficult to obtain, or a normalized method is wanted.

The improvements in detection performance for the multilook methods compared to prewhitening are significant when acoustic noise dominates speckle, as illustrated in Figs. 17 and 18. Such a scenario is realistic as the imaging depth increases. The NMFW and NMF methods perform especially well in this scenario. They incorporate prior knowledge about the theoretical point signal response in each sublook and can weight the sublook accordingly.

Table 2 summarizes the observed benefits and setbacks of the suggested methods in this study.

7. Conclusions

We have studied four multilook methods with the aim of improving point detection in textured ultrasound images. The results

Table 2
Summary of observed potential benefits and setbacks of the suggested methods.

Scenario	Method				
	Prewhitening	MLCF	MLCFW	NMF	NMFW
Optimal whitening & optimal TC	Large improvement in detection performance.	Similar performance as whitening.	Similar performance as whitening. Slightly better than whitening in the case of large texture.	Setback compared to whitening.	Similar performance as whitening.
Suboptimal prewhitening wo/texture	Some reduction in detection performance, but still a robust method.	Performs slightly better than whitening.	Performs slightly better than whitening.	Performs slightly better than whitening.	Performs better than whitening.
Suboptimal prewhitening w/texture	Some reduction in detection performance, but still a robust method.	Similar performance as whitening.	Performs slightly better than whitening at low P_{FA} values.	Some setback compared to whitening.	Performs slightly better than whitening at low P_{FA} values.
Wide prewhitening w/texture	Reduction in detection performance.	Similar performance as whitening.	Similar performance as whitening.	Performs slightly better than whitening at low P_{FA} values.	Performs better than whitening.
Suboptimal TC	Much affected by suboptimal TC.	Not affected by TC.	Improvement due to weighting with MLCF.	Not affected by TC.	Improvement due to weighting with NMF.
Poor TC	Much affected by poor TC.	Not affected by TC.	Affected by poor TC.	Not affected by TC.	Affected by poor TC.
Dominant additive acoustic noise	Improvement compared to only TC, but method enhances much of the noise.	Method weights sublooks using coherence.	Method weights sublooks using coherence.	Method weights sublooks according to theoretical point signal response.	Method weights sublooks according to theoretical point signal response.
Computational complexity	Low	Medium	Medium	High	High

Color coding:	Poor		Good		Great

show *significant* improvement in detection performance using optimized prewhitening on images where an optimal texture correction is easily obtained. An improvement in detection performance is also found for the image weighting multilook method MLCFW. When detecting point targets in textured backgrounds, the multilook methods require sublooks with higher image resolution than in uniform backgrounds. In general, the methods perform best when using many sublooks with high image resolution. The optimal number of sublooks depend on the texture size. The methods in this study perform best on the images with slowly varying texture. The NMF and MLCF methods are normalized and perform better than prewhitening when an optimal texture correction is difficult to obtain. The multilook methods perform better than prewhitening when acoustic noise dominates the speckle background.

Declaration of competing interest

The authors declare that they have no known competing financial interests or personal relationships that could have appeared to influence the work reported in this paper.

Data availability

Data will be made available on request.

References

[1] M.E. Anderson, M.S. Soo, R.C. Bentley, G.E. Trahey, The detection of breast microcalcifications with medical ultrasound, J. Acoust. Soc. Am. 101 (1) (1997) 29–39, http://dx.doi.org/10.1121/1.417973.

[2] M.E. Anderson, M.S.C. Soo, G.E. Trahey, Microcalcifications as elastic scatterers under ultrasound, IEEE Trans. Ultrason. Ferroelectr. Freq. Control 45 (4) (1998) 925–934, http://dx.doi.org/10.1109/58.710559.

[3] M.E. Anderson, M.S.C. Soo, G.E. Trahey, Optimizing visualization of breast microcalcifications, in: Proc. IEEE Int. Ultrason. Symp. (IUS), Vol. 2, 2000, pp. 1315–1320, http://dx.doi.org/10.1109/ULTSYM.2000.921565.

[4] P. Machado, J.R. Eisenbrey, M. Stanczak, B.C. Cavanaugh, L.M. Zorn, F. Forsberg, Ultrasound detection of microcalcifications in surgical breast specimens, Ultrasound Med. Biol. 44 (2018) 1286–1290, http://dx.doi.org/10.1016/j.ultrasmedbio.2018.02.009.

[5] E. Flørenæs, S. Solberg, J. Kvam, O.F. Myhre, O.M. Brende, B. Angelsen, In vitro detection of microcalcifications using dual band ultrasound, in: Proc. IEEE Int. Ultrason. Symp., IUS, 2017, pp. 1–4, http://dx.doi.org/10.1109/ULTSYM.2017.8092857.

[6] R. Guo, G. Lu, B. Qin, B. Fei, Ultrasound imaging technologies for breast cancer detection and management: A review, Ultrasound Med. Biol. 44 (1) (2018) 37–70, http://dx.doi.org/10.1016/j.ultrasmedbio.2017.09.012.

[7] A.A. Ray, D. Ghiculete, K.T. Pace, R.J.D. Honey, Limitations to ultrasound in the detection and measurement of urinary tract calculi, Urology 76 (2) (2010) 295–300, http://dx.doi.org/10.1016/j.urology.2009.12.015.

[8] J.E. Tierney, S.G. Schlunk, R. Jones, M. George, P. Karve, R. Duddu, B.C. Byram, R.S. Hsi, In vitro feasibility of next generation non-linear beamforming ultrasound methods to characterize and size kidney stones, Urolithiasis 47 (2018) 181–188, http://dx.doi.org/10.1007/s00240-018-1036-z.

[9] J.E. Browne, D. King, A.J. Fagan, D. Chari, C.M. Moran, An investigation of the detection capability of pulsed wave duplex Doppler of low grade stenosis using ultrasound contrast agent microbubbles – An in-vitro study, Ultrasonics 96 (2019) 48–54, http://dx.doi.org/10.1016/j.ultras.2019.04.003.

[10] C. Pellow, J. Tan, E. Chérin, C.E. Demore, G. Zheng, D.E. Goertz, High frequency ultrasound nonlinear scattering from porphyrin nanobubbles, Ultrasonics 110 (2021) 106245, http://dx.doi.org/10.1016/j.ultras.2020.106245.

[11] G. Matrone, M.A.L. Bell, E. Gonzalez, A. Ramalli, Short-lag spatial coherence imaging with multi-line transmission to improve needle visibility in ultrasound images, J. Acoust. Soc. Am. 146 (2019) 2861, http://dx.doi.org/10.1121/1.5136925.

[12] G. Matrone, M.A.L. Bell, A. Ramalli, Improving the detectability of highly coherent targets in short-lag spatial coherence images with multi-line transmission, in: Proc. IEEE Int. Ultrason. Symp., IUS, 2020, pp. 1–4, http://dx.doi.org/10.1109/IUS46767.2020.9251371.

[13] K. Diamantis, A.H. Greenaway, T. Anderson, J.A. Jensen, P.A. Dalgarno, V. Sboros, Super-resolution axial localization of ultrasound scatter using multi-focal imaging, IEEE Trans. Biomed. Eng. 65 (8) (2018) 1840–1851, http://dx.doi.org/10.1109/TBME.2017.2769164.

[14] S.H. Thon, R.E. Hansen, A. Austeng, Point detection in ultrasound using prewhitening and multilook optimization, IEEE Trans. Ultrason. Ferroelectr. Freq. Control 69 (6) (2022) 2085–2097, http://dx.doi.org/10.1109/TUFFC.2022.3167923.

[15] M. Sakhaei, A. Mahloojifar, A. Malek, Optimization of point spread function in ultrasound arrays, Ultrasonics 44 (2) (2006) 159–165, http://dx.doi.org/10.1016/j.ultras.2005.10.002.

[16] R. Czerwinski, D. Jones, W. O'Brien, Line and boundary detection in speckle images, IEEE Trans. Image Process. 7 (12) (1998) 1700–1714, http://dx.doi.org/10.1109/83.730381.

[17] R. Czerwinski, D. Jones, W. O'Brien, Detection of lines and boundaries in speckle images-application to medical ultrasound, IEEE Trans. Med. Imaging 18 (2) (1999) 126–136, http://dx.doi.org/10.1109/42.759114.

[18] J.A. Jensen, N.B. Svendsen, Calculation of Pressure Fields from Arbitrarily Shaped, Apodized, and Excited Ultrasound Transducers, IEEE Trans. Ultrason. Ferroelectr. Freq. Control 39 (2) (1992) 262–267, http://dx.doi.org/10.1109/58.139123.

[19] J.A. Jensen, FIELD: A Program for Simulating Ultrasound Systems, in: Proc. 10th Nordicbaltic Conf. Biomed. Imag., Suppl. 1, Part 1, Vol. 4, 1996, pp. 351–353.

[20] J.A. Jensen, S.I. Nikolov, K.L. Gammelmark, M.H. Pedersen, Synthetic aperture ultrasound imaging, Ultrasonics 44 (2006) e5–e15, http://dx.doi.org/10.1016/j.ultras.2006.07.017.

[21] T.L. Szabo, Diagnostic Ultrasound Imaging: Inside Out, second ed., Elsevier, Amsterdam, The Netherlands, 2014, http://dx.doi.org/10.1016/C2011-0-07261-7.

[22] E. Conte, M. Lops, G. Ricci, Asymptotically optimum radar detection in compound-Gaussian clutter, IEEE Trans. Aerosp. Electron. 31 (2) (1995) 617–625, http://dx.doi.org/10.1109/7.381910.

[23] E. Conte, M. Lops, G. Ricci, Adaptive matched filter detection in spherically invariant noise, IEEE Signal Process. Lett. 3 (8) (1996) 248–250, http://dx.doi.org/10.1109/97.511809.

[24] E.J. Kelly, An adaptive detection algorithm, IEEE Trans. Aerosp. Electron. 22 (2) (1986) 115–127, http://dx.doi.org/10.1109/TAES.1986.310745.

[25] M.J. Sanjuan-Ferrer, I. Hajnsek, K.P. Papathanassiou, A. Moreira, A new detection algorithm for coherent scatterers in SAR data, IEEE Trans. Geosci. Remote Sens. 53 (11) (2015) 6293–6307, http://dx.doi.org/10.1109/TGRS.2015.2438173.

[26] H. Masoom, R.S. Adve, R.S. Cobbold, Target detection in diagnostic ultrasound: Evaluation of a method based on the CLEAN algorithm, Ultrasonics 53 (2) (2013) 335–344, http://dx.doi.org/10.1016/j.ultras.2012.06.016.

[27] J.C.V. Jakowatz, D.E. Wahl, P.H. Eichel, D.C. Ghiglia, P.A. Thompson, Spotlight-Mode Synthetic Aperture Radar: A Signal Processing Approach, Springer, Boston, MA, 1996.

[28] C. Oliver, S. Quegan, Understanding Synthetic Aperture Radar Images, SciTech Publishing, Raleigh, NC, USA, 2004.

[29] S.M. Kay, Fundamentals of Statistical Signal Processing, Volume II: Detection Theory, Vol. II, Prentice-Hall PTR, Upper Saddle River, NJ, USA, 1998.

[30] S. Hverven Thon, R.E. Hansen, A. Austeng, Detection of point scatterers in medical ultrasound, IEEE Trans. Ultrason. Ferroelectr. Freq. Control 69 (2) (2022) 617–628, http://dx.doi.org/10.1109/TUFFC.2021.3129619.

[31] B.C. Levy, Principles of Signal Detection and Parameter Estimation, Springer, Boston, MA, USA, 2008.

[32] D.A. Abraham, Underwater Acoustic Signal Processing: Modeling, Detection, and Estimation, Springer, Cham, Switzerland, 2019, http://dx.doi.org/10.1007/978-3-319-92983-5.

[33] J.A. Hanley, B.J. McNeil, The meaning and use of the area under a receiver operating characteristic (ROC) curve, Radiology 143 (1) (1982) 29–36, http://dx.doi.org/10.1148/radiology.143.1.7063747.

[34] S.M. Alessio, Digital Signal Processing and Spectral Analysis for Scientists, Springer, Cham, Switzerland, 2016.

[35] H.-C. Shin, R. Prager, J. Ng, H. Gomersall, N. Kingsbury, G. Treece, A. Gee, Sensitivity to point-spread function parameters in medical ultrasound image deconvolution, Ultrasonics 49 (3) (2009) 344–357, http://dx.doi.org/10.1016/j.ultras.2008.10.005.

[36] C. Chen, H.H.G. Hansen, G.A.G.M. Hendriks, J. Menssen, J.-Y. Lu, C.L. de Korte, Point spread function formation in plane-wave imaging: A theoretical approximation in Fourier migration, IEEE Trans. Ultrason. Ferroelectr. Freq. Control 67 (2) (2020) 296–307, http://dx.doi.org/10.1109/TUFFC.2019.2944191.

[37] M.E. Anderson, G.E. Trahey, A seminar on k-space applied to medical ultrasound, 2000, URL: https://www.researchgate.net/profile/Gregg-Trahey/publication/267974609_A_seminar_on_k_-space_applied_to_medical_ultrasound/links/54bd30c00cf27c8f2814b1d0/A-seminar-on-k-space-applied-to-medical-ultrasound.pdf.

[38] C. Golfetto, I.K. Ekroll, H. Torp, L. Løvstakken, J. Avdal, Retrospective transmit beamforming and coherent plane-wave compounding for microvascular Doppler imaging: A comparison study, IEEE Trans. Ultrason. Ferroelectr. Freq. Control 68 (4) (2021) 1105–1116, http://dx.doi.org/10.1109/TUFFC.2020.3033719.

[39] B. Denarie, T.A. Tangen, I.K. Ekroll, N. Rolim, H. Torp, T. Bjåstad, L. Lovstakken, Coherent plane wave compounding for very high frame rate ultrasonography of rapidly moving targets, IEEE Trans. Med. Imaging 32 (7) (2013) 1265–1276, http://dx.doi.org/10.1109/TMI.2013.2255310.

[40] A. De Maio, G. Fornaro, A. Pauciullo, Detection of single scatterers in multidimensional SAR imaging, IEEE Trans. Geosci. Remote Sens. 47 (7) (2009) 2284–2297, http://dx.doi.org/10.1109/TGRS.2008.2011632.

[41] A. Rodriguez-Molares, O.M.H. Rindal, O. Bernard, A. Nair, M.A.L. Bell, H. Liebgott, A. Austeng, L. Løvstakken, The UltraSound ToolBox, in: Proc. IEEE Int. Ultrason. Symp., IUS, 2017, pp. 1–4, http://dx.doi.org/10.1109/ULTSYM.2017.8092389.

[42] O.M.H. Rindal, A. Austeng, A. Fatemi, A. Rodriguez-Molares, The effect of dynamic range alterations in the estimation of contrast, IEEE Trans. Ultrason. Ferroelectr. Freq. Control 66 (7) (2019) 1198–1208, http://dx.doi.org/10.1109/TUFFC.2019.2911267.